

First Observations of Tracking Clouds Using Scanning ARM Cloud Radars

PALOMA BORQUE AND PAVLOS KOLLIAS

Department of Atmospheric and Oceanic Sciences, McGill University, Montreal, Quebec, Canada

SCOTT GIANGRANDE

Brookhaven National Laboratory, Upton, New York

(Manuscript received 28 May 2013, in final form 30 August 2014)

ABSTRACT

Tracking clouds using scanning cloud radars can help to document the temporal evolution of cloud properties well before large-drop formation (weather radar “first echo”). These measurements also complement cloud and precipitation tracking using geostationary satellites and weather radars. Here, two-dimensional (2D) along-wind range–height indicator observations of a population of shallow cumuli (with and without precipitation) from the 35-GHz scanning Atmospheric Radiation Measurement Program (ARM) cloud radar (SACR) at the U.S. Department of Energy (DOE)–ARM Southern Great Plains (SGP) site are presented. Observations from the ARM SGP network of scanning precipitation radars are used to provide the larger-scale context of the cloud field and to highlight the advantages of the SACR to detect the numerous small nonprecipitating cloud elements. A new cloud identification and tracking algorithm (CITA) is developed to track cloud elements. In CITA, a cloud element is identified as a region having a contiguous set of pixels exceeding a preset reflectivity and size threshold. The high temporal resolution of the SACR 2D observations (30 s) allows for an area superposition criteria algorithm to match cloud elements at consecutive times. Following CITA, the temporal evolution of cloud-element properties (number, size, and maximum reflectivity) is presented. The vast majority of the designated elements during this cumulus event were short-lived nonprecipitating clouds having an apparent life cycle shorter than 15 min. The advantages and disadvantages of cloud tracking using an SACR are discussed.

1. Introduction

Clouds play a critical role in Earth’s climate system through their participation in Earth’s radiation budget, the hydrological cycle, and the vertical redistribution of energy and moisture in the atmosphere (e.g., [Stephens 2005](#); [Feingold and Siebert 2009](#)). The accurate representation of the factors that control cloud microscale and macroscale properties in global climate models and cloud-resolving models remains a major challenge (e.g., [Ghan et al. 1999](#); [Grenier and Bretherton 2001](#); [Park and Bretherton 2009](#); [Stevens and Feingold 2009](#)). Continuously operating ground-based supersites ([Stokes and Schwartz 1994](#); [Ackerman and Stokes 2003](#); [Illingworth et al. 2007](#)) equipped with a wide range of active and

passive sensors provide detailed information on cloud dynamical and microphysical properties. Until recently, the cloud properties retrieved at these ground-based supersites were limited to the column sampled by profiling sensors. Now, scanning cloud and precipitation radars are deployed to provide information on the 3D structure of clouds and precipitation ([Mather and Voyles 2013](#); [Kollias et al. 2014a](#)). One of the main scientific drivers for deploying scanning cloud radars is the desire to document individual cloud elements as they transit through different stages of their life cycle (e.g., cloud formation, precipitation onset, dissipation). Relating the temporal evolution of cloud systems to aerosol and large-scale meteorology conditions could lead to a better understanding of the controls on low clouds and associated statistics.

Monitoring the temporal evolution of shallow cumulus clouds can be accomplished using ground-based and airborne-based radar systems (multiple passes). Capturing the early stage of cumulus development/detection (first

Corresponding author address: Paloma Borque, Department of Atmospheric and Oceanic Sciences, Room 945, Burnside Hall, 805 Sherbrooke Street West, Montreal QC H3A 2K6, Canada.
E-mail: paloma.borque@mail.mcgill.ca

echo) depends on the sensitivity of the radar system. When centimeter-wavelength radars have been tasked for these studies, the first echo coincides with the early development of small precipitation particles (Knight and Miller 1993; Knight et al. 2002; Göke et al. 2007; Burnet and Brenguier 2010). This early development of a precipitation echo implies that an efficient collision-coalescence process drives particle growth in warm clouds. French et al. (1999) used multiple passes over shallow cumulus clouds and observations from an airborne millimeter-wavelength radar to document the temporal evolution of nonprecipitating cumulus clouds. These early efforts demonstrate the potential of scanning radars to monitor the temporal evolution of shallow cumuli. However, the studied dataset are limited and, in the majority of the studies, the use of centimeter-wavelength radars does not permit the documentation of the cloud life cycle before the development of small raindrop particles. The spatial and temporal resolution of geostationary satellites also limits their applicability for the detection of small, nonprecipitating cumuli clouds.

The deployment of continuously operating scanning cloud radars (Mather and Voyles 2013; Kollias et al. 2014a) at the U.S. Department of Energy (DOE) Atmospheric Radiation Measurement (ARM) Program fixed and mobile sites offers the required observational capabilities for monitoring the entire life cycle of shallow cumuli clouds over an extensive period of time. This is particularly germane for the ARM Southern Great Plain (SGP) facility that is equipped with a distributed multifrequency scanning radar network. This network includes a scanning ARM cloud radar (SACR) with sensitivity (~ -30 dBZ at 10 km) and spatial (45 m) and temporal resolution (~ 30 s per horizon-to-horizon scan) sufficient for continuous tracking of nonprecipitating short-lived cloud elements.

Here, we present the first set of observations from this scanning cloud radar facility during a warm season cloud event with a wide distribution of cloud types from short-lived, nonprecipitating cumuli to shallow light precipitating cumulus clouds. The details of a cloud identification and tracking algorithm (CITA) suitable for monitoring the evolution of shallow cumulus in a range-height indicator (RHI) plane are presented. Preliminary statistics of the temporal gradient of the radar reflectivity in shallow nonprecipitating clouds are presented. The limitations and capabilities of the ARM SGP facility to study the life cycle of cloud elements are discussed.

2. Observations

The observations presented in this study were collected during the Midlatitude Continental Convective

Clouds Experiment (MC3E) conducted in April–June 2011 at the ARM SGP facility. MC3E was the result of a collaborative effort between the DOE–ARM Program and its Climate Research Facility and the National Aeronautics and Space Administration’s Global Precipitation Measurement mission Ground Validation program. The MC3E campaign was the first major field experiment conducted at an ARM site after the acquisition of the new scanning ARM radar (Fig. 1; Mather and Voyles 2013). The backbone infrastructure of the ARM SGP radar facility is a distributed heterogeneous network of profiling and scanning radar systems suitable for the mapping of cloud and precipitation in 3D along with a small network of radiometers and lidars. The SGP radar facility includes a 5.4-GHz (5.5-cm wavelength) C-band scanning ARM precipitation radar (C-SAPR), a network of three 9.4-GHz (3.2-cm wavelength) X-band scanning ARM precipitation radars (X-SAPR), and a dual-frequency 35.3–93.9-GHz (8.5–3.2 mm) scanning cloud radar (Ka-/W-SACR; Fig. 1).

The bulk of the observations presented in this manuscript are from the SACR located at the ARM SGP Central Facility (CF). A total sky imager (TSI), radiosonde launch facility, 2D video disdrometer, wind profiler, and a laser ceilometer are also present at the CF and are used in this study. The C-SAPR is located approximately 25 km to the north of the SGP CF, and the three X-SAPR systems are located in a triangular configuration having a side (baseline) of approximately 20 km and centered on the SGP CF (Fig. 1). The primary motivation for the C-SAPR polarimetric radar system is to provide the mesoscale context of precipitation over a 100–120-km domain range around the CF. The acquisition of the X-band radar network at the ARM SGP radar facility is based on the desire to bridge the observational gap in sensitivity and spatial scales between the dual-frequency scanning cloud radar and the C-band polarimetric radar. The SACR is a dual-frequency scanning Doppler and polarimetric radar. However, during the MC3E only the 35-GHz (Ka band) radar frequency was operational (Table 1). With sensitivity close to -30 dBZ at 10 km during nominal scanning parameters, the Ka-SACR is capable of detecting clouds from early formation stages. Additional details on the first generation of SACR operational strategies and data postprocessing are described in Kollias et al. (2014a,b) and section 3 of this study. The SACR scan strategy adopted for this event included horizon-to-horizon along-wind scans (AW-RHI), which require the primary wind direction at cloud level as an input. Once this wind direction is designated, the cloud radar is expected to capture the

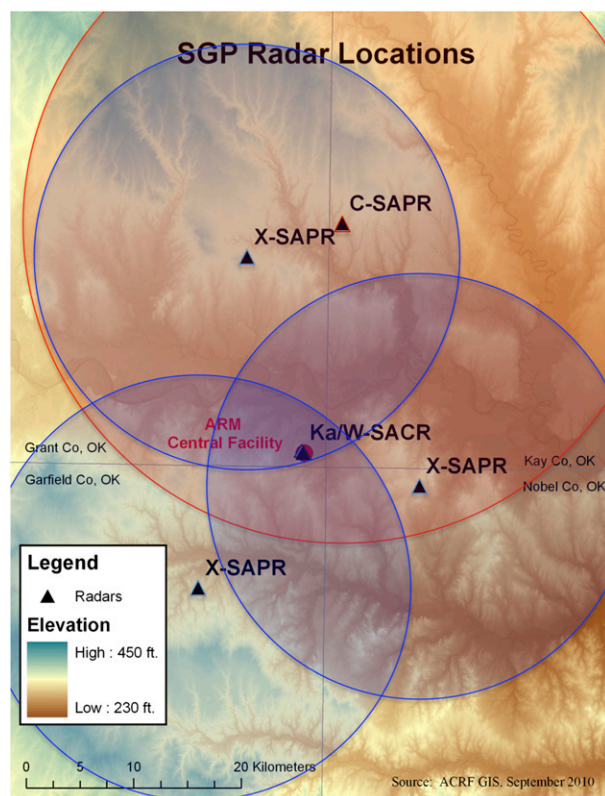


FIG. 1. Map showing the heterogeneous ARM radar network at the SGP facility. Blue rings indicate a 20-km radius around each X-band radar, and the red ring indicates a 30-km radius around the C-band radar.

evolution of the same cloud element as it is advected over the instrument.

For this particular case, the wind direction was determined by consulting the relevant 1730 UTC radiosonde, wind profiler, and visible satellite images available in real time by the authors in the field. This wind direction was also visually confirmed in situ by the authors and later corroborated by the 2030 UTC CF radiosonde. Furthermore, postevent inspection of the TSI, X-SAPR, and C-SAPR animations showed that the motion of more substantial clouds detected by these systems did not deviate substantially from the estimated flow. The radar scan direction (azimuth) was fixed for the duration of the Ka-SACR AW-RHI scan strategy period, although this was not a concern for interpretation of the clouds collected during the 2.5-h event window. Specifically, wind in the cloud layer did not suggest an appreciable change in time or height. Furthermore, no shear was apparent in radiosonde data that would suggest clouds moving differently at different heights (Fig. 2). However, a more detailed look at the importance of potential off-angle scanning is provided in the [appendix](#).

TABLE 1. Ka-SACR technical specifications.

Scanning ARM cloud radar (Ka band)	
Scan type	Along-wind horizon-to-horizon
Nyquist velocity	10.5 m s^{-1}
Range resolution	20 m
Scan time	~30 s
Pulse repetition frequency	5 kHz
Sensitivity	~-30 dB at 10 km
Frequency	35.29 GHz
Wavelength	8.5 mm

Figure 3 demonstrates the advantage of having a heterogeneous network of radars to document the temporal and spatial distribution of clouds from their early, low reflectivity stages to their more mature precipitation-associated regime and following lower reflectivity decay stage. This figure shows an example of data collected by the Ka-SACR, C-SAPR, and southeast X-SAPR at a time when primarily weak nonprecipitating clouds were present over SGP CF. The total sky imager (Fig. 3a) confirms the presence of shallow broken cumuli over the CF. These same clouds are observed by the Ka-SACR overhead (Fig. 3d). All ARM radars observe a precipitating shallow cumulus at a 5–10-km range from the Ka-SACR (southeast part of the AW-RHI scan). The SAPRs have difficulty detecting the nonprecipitating clouds observed by the Ka-SACR, illustrating the importance of millimeter radar observations for capturing shallow nonprecipitating clouds as well as the early stages of cloud evolution (Fig. 3). These sampling considerations are not only a consequence of the differences in radar wavelength, but also related other factors including beamwidth, relative cloud-to-radar distance, and scanning strategy.

3. Cloud identification and tracking algorithm

Several studies document the evolution of cloud systems, often with an emphasis on characterizing the life cycle and morphology of deep convective systems through the use of cloud tracking algorithms (e.g., Williams and Houze 1987; Velasco and Fritsch 1987; Rosenfeld 1987; Johnson et al. 1998; Dixon and Wiener 1993; Machado et al. 1998). Satellite-based cloud tracking studies identify deep convective cloud elements using infrared temperature thresholds (e.g., Maddox 1980; Williams and Houze 1987; Chen et al. 1996) and additional spatial coherency constraints (e.g., Machado et al. 1998; Futyan and Del Genio 2007). From the surface, radar-based cell designation and tracking algorithms capitalize on radar reflectivity factor patterns and additional size constraints (e.g., Dixon and Wiener 1993; Rosenfeld 1987; Johnson et al. 1998). These radar-based “cell” identifications act

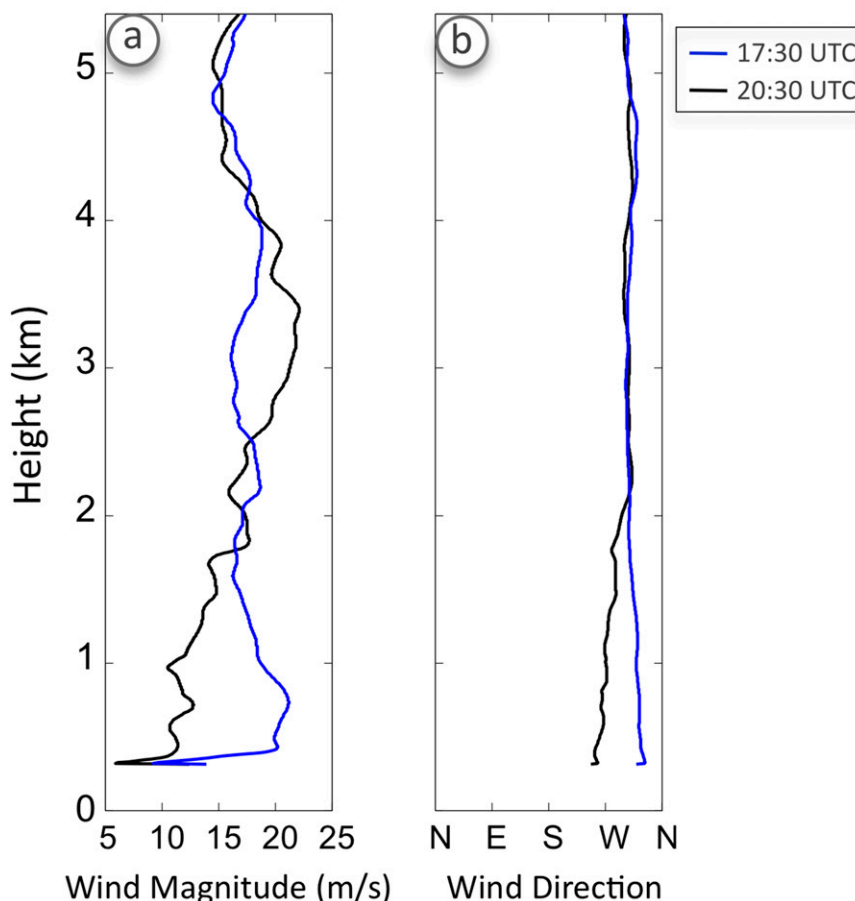


FIG. 2. Wind (a) magnitude and (b) direction from radiosonde observations at SGP CF at 1730 UTC (blue) and 2030 UTC (black) 25 May 2011.

as input for a tracking algorithm that connects the different stages of these cell patterns. This is often accomplished by determining area superposition between consecutive time steps (e.g., Williams and Houze 1987; Boer and Ramanathan 1997; Machado et al. 1998), cloud propagation speed and superposition (Rosenfeld 1987; Johnson et al. 1998; Futyán and Del Genio 2007), or by minimizing a cost function based on position and element volume differences at consecutive times (e.g., Dixon and Wiener 1993). For many deep convective cells and larger convective system examples as above, automatic and semiautomatic (manual selection of the optimal candidate) tracking algorithms often arrive at similar results (e.g., Machado et al. 1998).

The CITA was developed to analyze shallow cumulus clouds as they transit through different stages of their lifetime. The input to CITA is 2D (range–height) Ka-SACR observations collected during AW-RHI scans (e.g., Fig. 3d). Range gates that contain no meteorologically significant detections have been removed using a signal-to-noise-ratio threshold technique (e.g., Kollias

et al. 2014b). Furthermore, conditional sampling using the linear depolarization ratio and radar reflectivity from the Ka-SACR, as well as the cloud-base height from a ceilometer, has been applied to classify and filter radar echoes associated with insects (Kollias et al. 2014b). Once these nonmeteorological radar returns are removed, each AW-RHI radar image is processed and CITA identifies a cloud element as those echoes having a contiguous set of pixels with reflectivity ≥ -50 dBZ and assigns them an identification number (ID). The reflectivity of -50 dBZ matches the Ka-SACR sensitivity at a 1-km range during nominal scanning operational conditions. While the Ka-SACR will not be able to detect such weak cloud echoes at longer distance from the radar, it is known that the Ka-SACR offers sufficient sensitivity to observe weak nonprecipitating clouds at extended range. To further eliminate spurious echo clusters (due to imperfect removal of radar noise-only range gates and insect returns), only those radar echoes having areal coverage larger than 0.5 km^2 are considered as cloud elements.

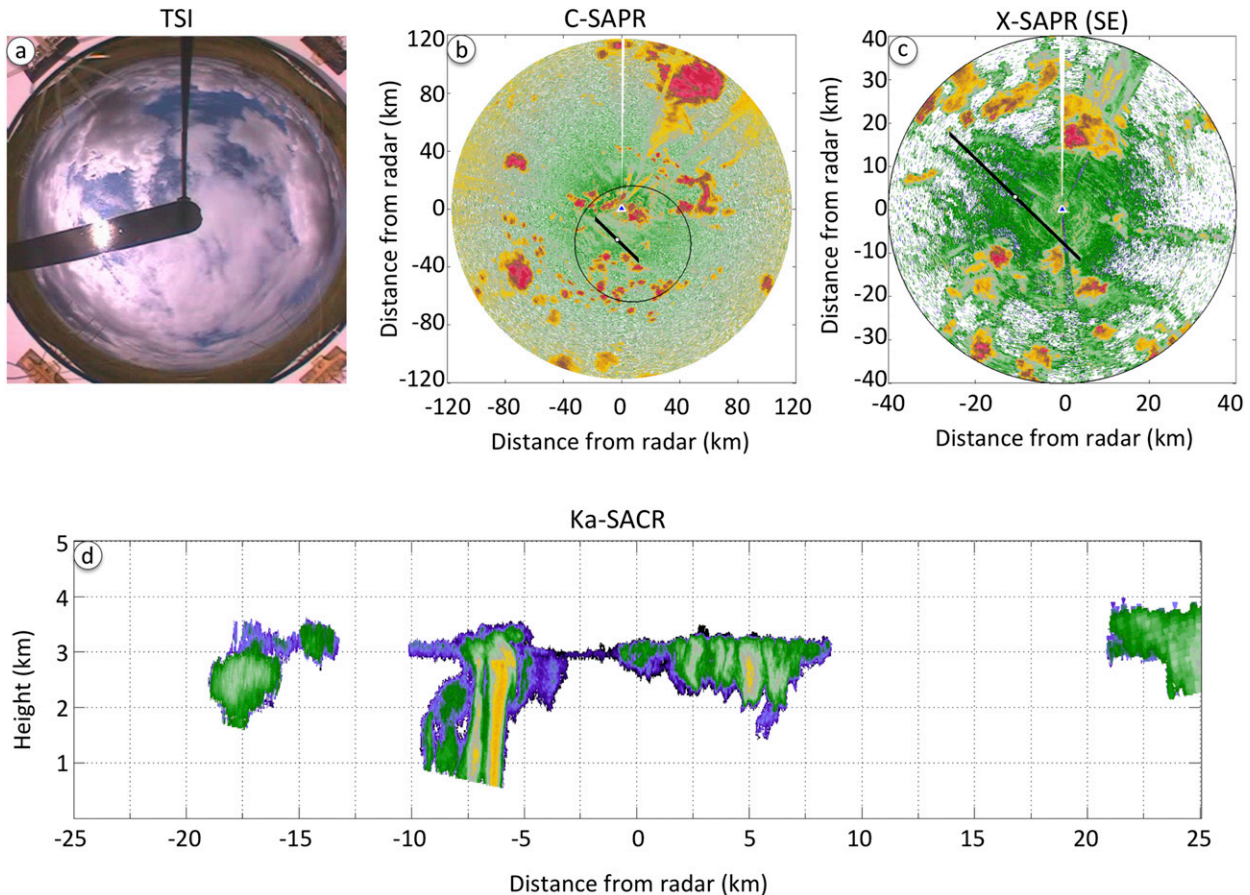


FIG. 3. (a) Hemispherical view of the cloud field at the Central Facility from the total sky imager and reflectivity from the (b) C-SAPR PPI scan at 1.2° at 2011 UTC and (c) X-SAPR PPI scan at 1.5° at 2010 UTC, and (d) Ka-SACR AW-RHI scan at 2010 UTC 25 May 2011 when weak mostly nonprecipitating clouds were present over the Central Facility. In (b) and (c), the triangle represents the location of the radar, the white dot represents the location of the Central Facility, the black line represents the SACR scan, and the black circle represents the domain over which SE X-SAPR data are collected. Orientation in (d) is NW on the right and SE on the left.

The second component of CITA is an application of a superposition criterion to track the temporal-spatial movement of each cloud ID assigned element (e.g., Figs. 4b,c). The superposition criterion identifies clusters that have the largest areal overlap in consecutive radar scans and assumes that these echoes represent the same cloud. This assumption is targeted at cloud data collected using AW-RHI SACR scanning that updates at 30-s intervals. When two cloud elements merge, the larger element retains the ID and continues forward in time, while the smaller cloud element and its associated ID is terminated. If a cloud element splits, the larger of the two elements continues in time with the previous tracking ID, while the smaller of the two elements is assigned a new ID. Basic evaluation for the validity of cloud merge and split events during this study was performed by the authors (e.g., manual checks for the time coherency in the range-height plane of cloud elements).

An example illustration of CITA for a sequence of three consecutive scans from Ka-SACR on 25 May 2011 is shown in Fig. 4. At the first time step, six cloud cells are identified by CITA (ID: 1–6). Cloud elements with IDs 1 and 4 show no merges or splits during this sequence (Fig. 4). Cloud elements assigned the IDs 2 and 3 (Fig. 4a) merge into a single cloud element assigned to a tracking ID 2 (Fig. 4b). Cloud ID 6 (Fig. 4b) splits, initiating a new cloud ID 7 (Fig. 4c). A more detailed look at the clouds illustrated in Fig. 4 is provided later in this section. For this MC3E observing period, the aforementioned CITA threshold and cloud interaction criteria were applied for the vast majority of the SACR dataset with apparent success (as visually confirmed by the authors). Any success from an echo overlap criteria (from fast updating AW-RHI modes) is beneficial as it eliminates the need to explore computationally demanding and less accurate tracking techniques. These other forms of trackers require an estimation of the cloud cell propagation speed

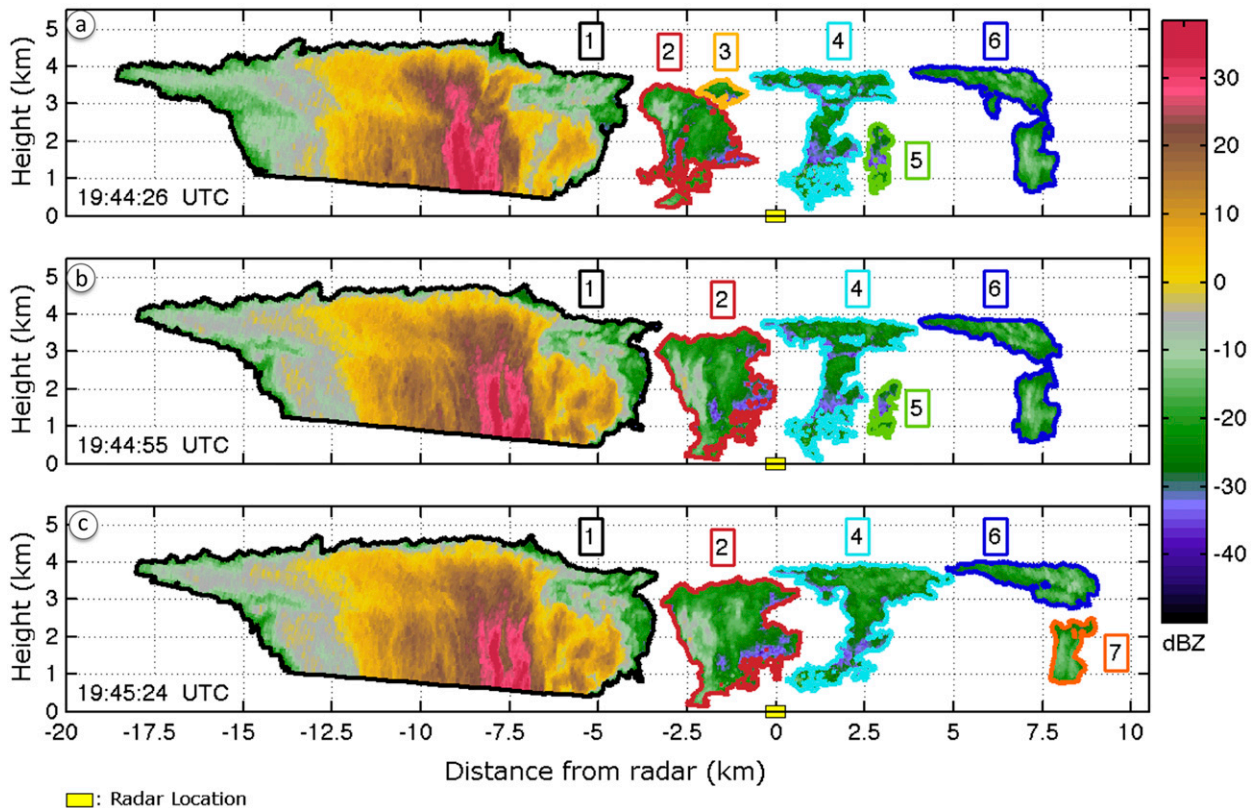


FIG. 4. Reflectivity from three consecutive Ka-SACR along-wind scans from 1944 to 1945 UTC (color shaded) and cloud identification numbers documented by the CITA (contours). Radar location is depicted by the yellow rectangle, and the time of each scan is indicated in the bottom left.

and/or the minimization of a cost function (based on previous position and volume) to overcome temporal gaps in cloud sampling.

Several sensitivity tests were performed to better evaluate the robustness of CITA results. As noted, this initial set of cloud elements and the associated cloud evolution behaviors presented in section 4 of this study were first manually inspected by the authors. Another simple test of algorithm repeatability was also performed, wherein CITA was applied to this dataset in reverse temporal order. When applied in reverse, CITA demonstrated very similar ID counts and cell tracking results according to parameters to be discussed in section 4. The sensitivity of CITA to different cloud detection reflectivity factor thresholds was also tested for this event. Our analysis indicated that for reflectivity thresholds between -40 and -50 dBZ, there was no significant change in the number of clouds detected by the CITA approach or in the associated cloud primary microphysical or geometrical properties (Fig. 5). However, when more restrictive thresholds were applied, the implications for tracking and cloud parameter behavior were more pronounced for this event.

As one example, higher reflectivity thresholds had a noticeable impact on the tracking of a model-friendly parameter such as the maximum cloud reflectivity factor. During this MC3E event, we often observed cloud elements that exhibit multiple maxima regions, as consistent with multiple coherent precipitation shafts embedded within regions of lower cloud reflectivity. When the more restrictive thresholds (e.g., those closer to values from the literature indicative of the presence of drizzle particles ~ -10 dBZ) were applied, multicored cloud elements were often divided by CITA and reclassified as unique cloud elements. Since this study emphasizes the tracking and evolution of individual cloud elements that may contain multiple precipitation cores, thresholds closer to -50 dBZ were those most appropriate to maintain the majority of the individual cloud forms.

Although low reflectivity thresholds were apparently necessary to maintain the majority of the cloud elements, lower thresholds sometimes presented difficulties when interpreting CITA outputs and the interaction between different cloud elements. Inspection of longer time sequences of cloud elements such as in Fig. 4

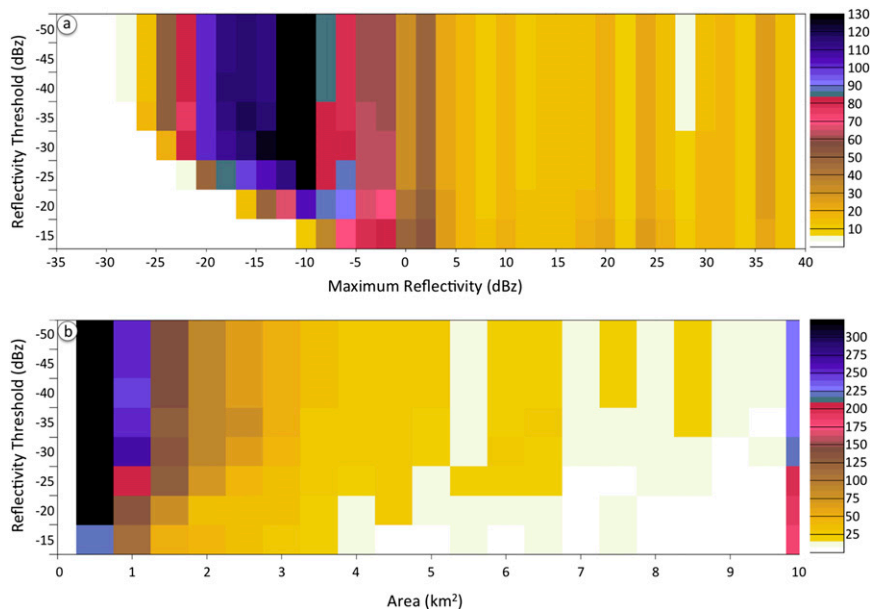


FIG. 5. (a) Maximum reflectivity frequency (bin: 2 dB) and (b) cloud area cross-section frequency (bin: 0.5 km²) for different reflectivity detection thresholds in CITA for the 25 May 2011 case.

illustrates many additional challenges faced by any identification and tracking algorithm requiring the selection of a reflectivity threshold. For example, from Fig. 4 it is interesting to note that CITA IDs 2, 4, and 6 were originally associated with low cumulus clouds having tops capped at approximately 2.5 km as early as 1940 UTC. These cloud-top heights were consistent with the height of the top of the environmental boundary layer (from available campaign collocated soundings). At the time of Fig. 4a, these shallow clouds had already merged with a population of developing higher-topped clouds (cloud tops near 4.5 km, in agreement with the environmental freezing level). These clouds had an initial vertical extent of ~ 1 km, similar to that observed with cloud ID 6 from Fig. 4c. With a more stringent reflectivity threshold, cloud IDs 6 and 7 in Fig. 4c may have survived as two distinct cloud levels. The current CITA tracking result depicts these clouds as artificially connected in the vertical, thus forming apparently more substantial clouds that split very shortly thereafter. However, more restrictive thresholds would come at the cost of lessened sampling of all cloud properties, with clear biases toward higher mean reflectivity values, smaller cloud elements and added deficiencies in documenting cloud initiation and decay. Area thresholds for cloud elements also act to mitigate select cloud IDs that might otherwise originate from splits or poor cumulus cloud RHI sampling–chording. Overall, the discussion on CITA threshold choice reflects trade-offs between capturing cloud entities (first echo initiation and subsequent

boundaries) and the ability to unambiguously distinguish different cloud entities for possible automatic settings. In this regard, it may be advisable to consider expert oversight so as to carefully analyze or tailor case or cloud-regime-specific thresholds accordingly.

4. Results

Using Ka-SACR observations from 25 May 2011 CITA identified a total of 1323 cloud elements. Of these elements, 49 (3.7%) were lost to a merger and 50 (3.78%) were the result of a split. In total, CITA was able to distinguish 338 distinct cloud life cycles (Fig. 6). This indicates that the vast majority of the cloud elements identified by CITA often corresponded to clouds detectable over only one unique time step. During this period, CITA tracked three long-lived shallow cloud elements (having cloud tops below 5 km) that persisted for more than 25 min. These clouds attained maximum reflectivity values exceeding 20 dBZ with cloud cross-sectional areas in excess of 40 km² during most of their observed cloud life cycle (Fig. 6). The majority of the shallow cloud elements were short-lived features. In many instances, CITA tracking indicated that the clouds lasted under 10 min and exhibited low maximal reflectivity cores (< -5 dBZ; see Figs. 6 and 7). Often, weaker cloud elements were observed to dissipate (or exit the domain) within 5 min of first detection. Once again, the confirmation that these echoes originated from clouds was provided by author in-field

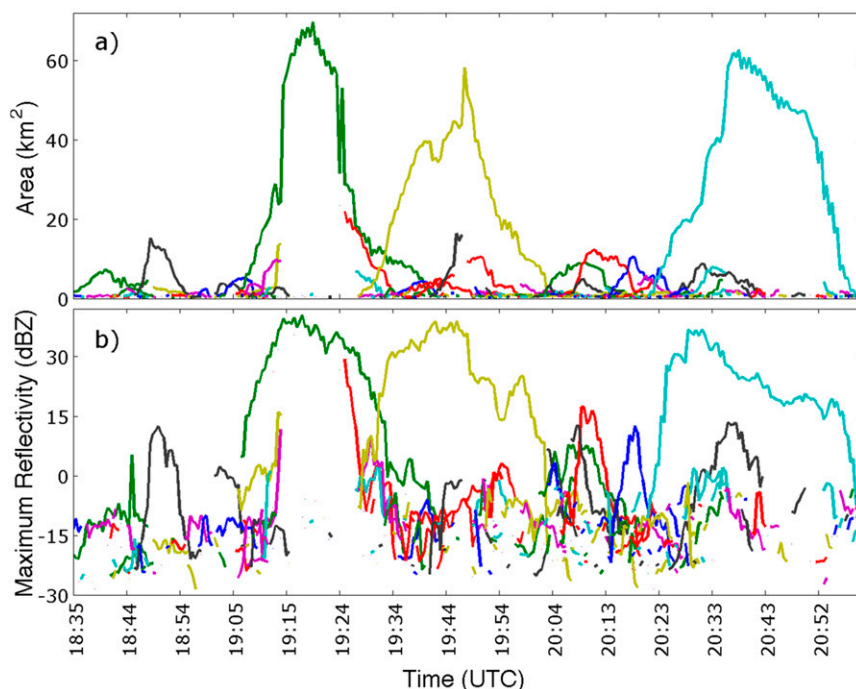


FIG. 6. (a) Cross-sectional area and (b) maximum reflectivity as a function of time for every element detected by the CITA on 25 May 2011 during the 2.5-h window. Colors represent individual clouds tracked by CITA.

observations, sounding evidence, surface TSI camera imagery, and an absence of stronger echoes in the SAPR imagery near the cloud radar scanning transect during most periods of observation.

The distribution of the maximum radar reflectivity values (for all 338 cloud elements detected within the Ka-SACR sampling window) is offered in Fig. 7a. This plot indicates that the majority of the cloud elements attain a maximum radar reflectivity between -20 and -10 dBZ (Fig. 7a). This magnitude of radar reflectivity at the SGP location in central Oklahoma is consistent with clouds that do not produce drizzle (Lu et al. 2008). The frequency distribution of the maximum cloud cross-sectional area peaks at the smallest possible detectable area coverage (CITA's size threshold of 0.5 km^2).

Additional geometrical properties for the identified cloud elements are also documented by CITA as a function of time. These parameters include the number of cloud elements, the cloud-element-top height and the maximum horizontal length of the cloud elements. The behaviors of these fields observed by the Ka-SACR for the 25 May event are provided in Fig. 8. During times of precipitation in the vicinity of the cloud radar [approximately 1920, 1950, and 2040 UTC, Fig. 8e, as observed using ARM disdrometer observations at the SGP CF as well as C-SAPR $R(Z)$ rainfall estimates averaged over the Ka-SACR scanning path], there are signs that

only cumulus cloud elements (Fig. 8b) with extended horizontal lengths (Fig. 8c) and higher relative top heights (Fig. 8d) are present. In contrast, there is a suggestion of a strongly bimodal or occasionally more complex distribution of cloud-top heights, most having shorter cumulus horizontal length scales, within the nonprecipitating and weaker initiating times. During these sequences (that includes times at the beginning of the observation period), one can consistently observe clouds having tops ranging from the lower levels around 2 km (in association with the top of the boundary level) up to higher cloud-top levels near 4 km (associated with the freezing level), within the same scan. Yet, when considering the periods associated with the onset or nearby precipitation, the complexity of these tracked parameters is often reduced and cloud tops below 2 km disappear, leaving sequences characterized mostly by cloud elements with elevated tops.

One plausible explanation for this bimodal cloud-top distribution relates to the evolution of the cloud field and its associated dynamics. The event started with exclusively shallow cumulus clouds over the SGP CF that later transitioned to congestus clouds comingled with lingering shallow cumulus. Therefore, the multilevel cloud-top structure is likely to be a combination of very shallow nonprecipitating mode, with some deeper precipitating cumulus. In times when these precipitating

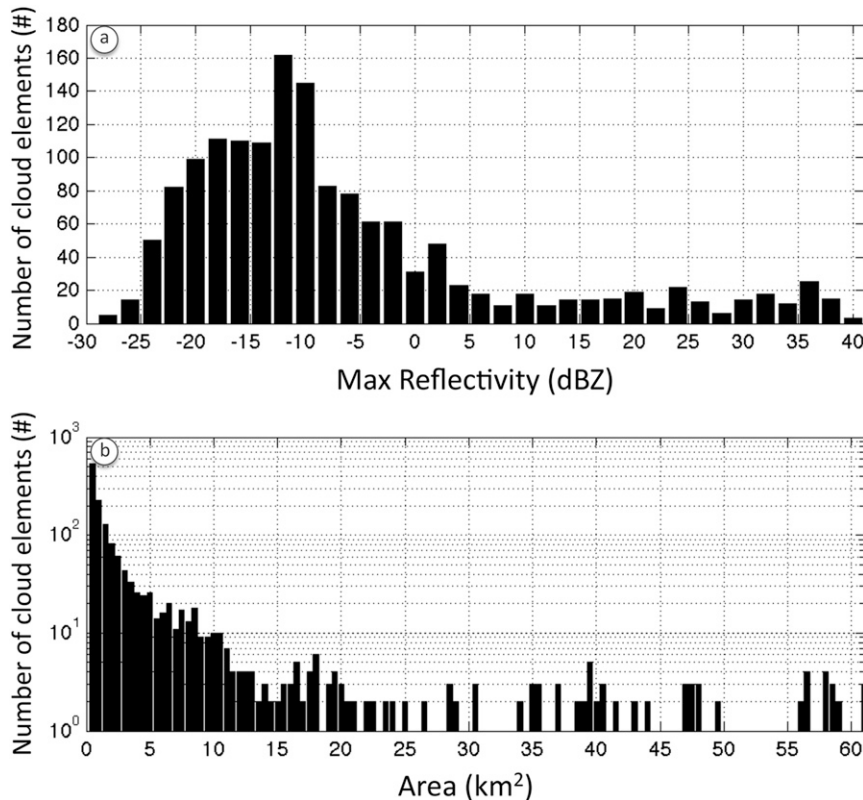


FIG. 7. Histogram of (a) maximum reflectivity and (b) area of all cloud elements detected by CITA for the 25 May 2011 case.

congustus clouds dominate the near vicinity of the radar (approximately 1920, 1950, and 2040 UTC), the associated cold-pool-type outflows [noticeable from the drop in equivalent potential temperature at SGP CF (see Fig. 8c), as well as X-SAPR and C-SAPR imagery] effectively act in a capacity to deter lower-topped shallow, surface-forced convection. This temporarily reduces the shallow-topped cloud observations for extended windows of atmospheric recovery.

An additional attempt to explore time-evolving cloud maximum and median properties and the associated local rate of change (as potentially related to cloud microphysical process and cloud growth and decay therein) is offered. The evolution of cloud radar reflectivity fields from discrete shallow nonprecipitating cloud target examples are provided in Fig. 9. To ensure these as discrete nonprecipitating cumuli conditions, the maximum and median parameter calculations and associated rate of change estimates are limited to only those calculations from the individual cloud elements that persist for a minimum of 5 min and have a maximum radar reflectivity that does not exceed -5 dBZ during the CITA cloud life-cycle tracking. As an additional constraint, we

restrict the dataset to only those “pure,” or discrete, cloud elements for which the CITA IDs have not experienced a merge or split. The remaining set of clouds are checked to ensure that a maximum in the radar reflectivity factor in time occurs at least three time steps after (before) the initial (final) detection by CITA. This latter constraint is intended to mitigate the inclusion of clouds that initiate too close to the edge of the Ka-SACR scanning domain and might propagate out of the domain before achieving a mature state. This also avoids mature clouds entering the edge of the scanning domain for which initiation or growth stages are not captured.

For these Fig. 9 demonstrations, it is observed that the local growth and/or decay rates of the maximum reflectivity are typically <10 dBZ min^{-1} . These also exhibit no clear relationship between the maximum reflectivity and its local rate of change for the surrounding minute of radar observations (Figs. 9a,b). Median cloud reflectivity values and the associated local rates of change are more gradual and demonstrate a maximum of 5 dBZ min^{-1} (Figs. 9c,d). Similarly, this local rate of change is likely to be independent of the median reflectivity value. In contrast to the maximum,

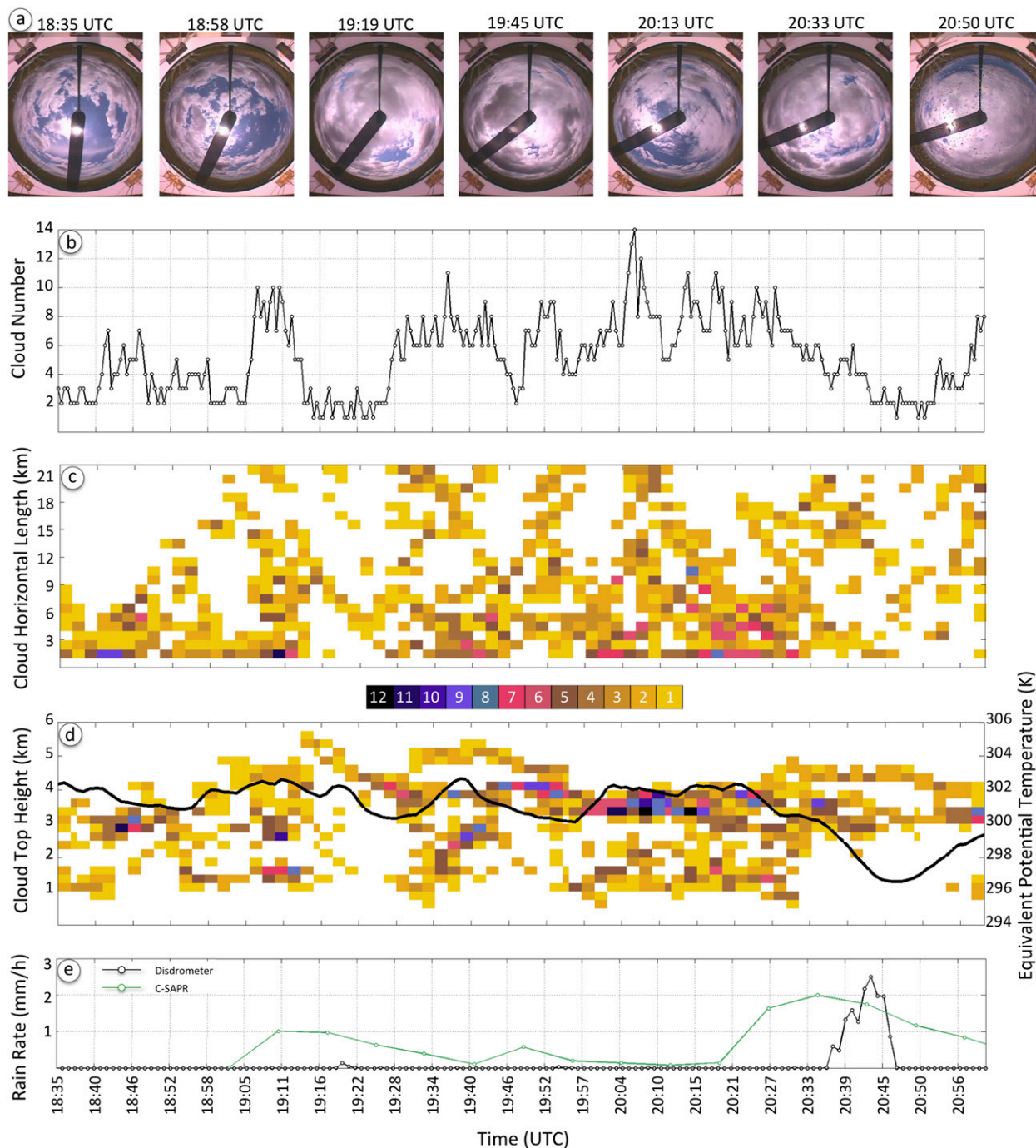


FIG. 8. (a) A sequence of TSI images during the 2.5-h-long observing period; (b) the number of cloud elements observed in the Ka-SACR AW-RHI scans, (c) the histogram of detected maximum cloud horizontal length from the Ka-SACRs, and (d) the histogram of detected cloud-top heights from the Ka-SACR and CF surface equivalent potential temperature, as functions of time; and (e) rain-rate estimations from the C-SAPR and the ARM disdrometer.

the median value and its relationship to its local rate of change is shown to be strongly tied to relative location of the cloud element to the radar location, wherein lower magnitudes of the median are observed closer to the radar

location (Figs. 9b–d). This is an obvious consequence of cloud elements having reduced radar sensitivity with range because of increased range gate volume with distance from radar. The influence of radar sensitivity is

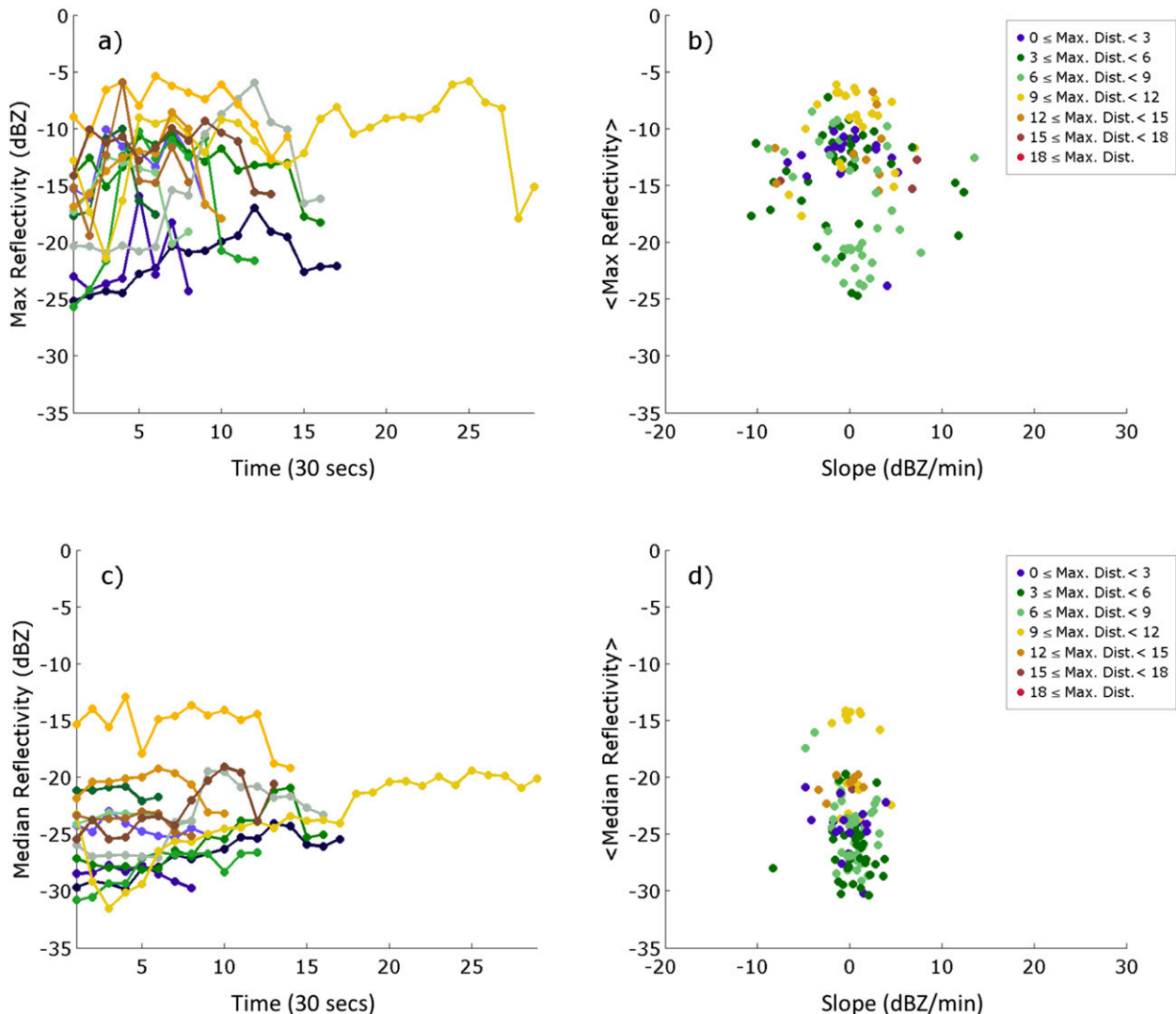


FIG. 9. (a) Temporal evolution of maximum reflectivity for shallow cumuli and (b) the rate of change of maximum reflectivity using a 1-min averaging window as a function of the mean maximum reflectivity over the segment where the rate of change was computed for small shallow cumulus clouds over SGP on 25 May 2011. (c),(d) As in (a) and (b), but for median reflectivity. For (b) and (d), the color code indicates the maximum distance between the cloud-element outer edge and the radar location (km).

larger if considering the evolution of the mean cloud reflectivity and its local rate of change (not shown). This indicates a limited relationship between these parameters and their rate of change, thus showing the larger influence of radar sensitivity when analyzing the time evolution of the mean and median cloud reflectivity.

5. Discussion and conclusions

This paper offers preliminary findings toward the potential capability to track and document the life cycle of shallow and weak cumulus to drizzling and showery cumulus clouds using a scanning millimeter wavelength cloud radar. Whereas cloud radars typically exhibit

enhanced sensitivity for the detection of these low-level cloud features, the ability of the scanning ARM cloud radar millimeter-wavelength radar for detection of the particular shallow and nonprecipitating boundary layer clouds from this dataset was improved owing to a reduced signal-to-clutter ratio and suppressed coherent scattering (e.g., Kollias et al. 2007). An along-wind scan strategy (AW-RHI) was implemented during the MC3E campaign and included high temporal sampling to facilitate the following of transient cloud elements as they advect with the mean wind field over the SACR platform at the ARM Southern Great Plains Central Facility. The ARM SGP site during the MC3E campaign was home to a network of

complementary scanning precipitation radars, lidars, and collocated surface properties instrumentation that gave context to SACR observations. Simple morphological analysis of complementary reflectivity factor observations from the scanning radar facilities in particular helps to demonstrate the potential benefits for having multiwavelength radar facilities of various scanning coverage scales, or cloud observational “super-sites,” to help bridge gaps between different cloud scales. There are significant morphological implications when one is unable to capture the full dynamic range of clouds from the smallest scales that may be detected by the millimeter wavelength radar (SACR) to the larger scales covered by the centimeter radars (X- and C-SAPR).

To better demonstrate the capabilities of the ARM SACR systems for the documentation of shallow cumulus evolution, the radar-based cloud identification and tracking algorithm was developed. A goal for CITA was to explore the possibilities for a functional method to track key cloud microphysical and geometric parameters, including their evolution in time and space, which are of interest to detailed cloud process studies and cloud model evaluation. Basic sensitivity testing for our initial set of CITA parameter outputs revealed that the current CITA design is capable of reliably documenting cloud metrics, such as cloud-element counts, maximum radar reflectivity factor, and cloud geometric properties including cloud top and cross-sectional area. CITA was tested on a postfrontal shallow cumulus dataset collected by the SACR when performing along-wind scans during MC3E on 25 May 2011. This day exhibited a wide variety of cumulus cloud conditions and featured 2.5 h of uninterrupted rapid radar scanning rates, thereby allowing CITA to track clouds unambiguously with time (e.g., Figs. 6, 7). The vast majority of the cloud elements detected by CITA were short-lived with life cycles shorter than 10 min, most of them decaying after the first 5 min and exhibiting low maximal reflectivity cores.

Three long-lived cumulus clouds were captured during the collection period and attained high reflectivity values that can be associated with precipitation onset in the region. The associated time evolution captured by CITA is complex, yet potentially highlights the eventual suffocation of the previously surface-driven-sort shallow cumulus clouds (albeit those having additional larger-scale forcing in the postfrontal environment) in the vicinity of the Ka-SACR. Moreover, observations suggest that these deeper precipitation modes preceded sequences of higher-based nonprecipitating cumulus cloud over the site, with these higher-based clouds possibly influenced by downward mixing of dry air associated with

the preceding precipitation over or near the region. Overall, most precipitation-free times demonstrate interesting behaviors during the presented event, including bimodal or more complex distributions of low-level cumulus clouds in terms of cloud-top heights and of smaller relative horizontal lengths.

Additional interpretation of the CITA dataset outputs in the context of the 25 May 2011 MC3E event indicates most cloud elements reflect numerous shallow nonprecipitating clouds having a maximum radar reflectivity < -5 dBZ (near the traditional “first echo” limit of precipitation radars). These shallow cumuli were often observed to be short-lived. The time-varying behaviors of the maximum and median cloud reflectivity and local attempts to calculate associated rates of change for nonprecipitating shallow cumulus examples were less conclusive (e.g., Fig. 9). It is not surprising to note that in following the evolution of median (and mean) cloud-element reflectivity factors, the tracking must account for changes in the sensitivity of the radar to cloud echoes to be of much use. Nevertheless, following cloud maximum behaviors (less influenced by radar sensitivity issues) as tractable quantities for microphysical evolution of the clouds was also challenging to interpret. Echo maximums are found to evolve quite rapidly and significantly in magnitude for well-captured shallow nonprecipitating cloud echo elements, and within only a few minutes of observation.

As this is the first application of CITA, more datasets are needed to drive a more robust verification of the CITA methodology and to allow more comprehensive cloud statistics. The findings for this study are also limited to shallow cloud observations from the Oklahoma SGP ARM CF, although we anticipate the methods should translate well to other cloud radar facilities for similar low cloud conditions. Application of CITA in real time or field campaign settings is also however nontrivial and strongly tied to an ability to characterize the cloud-level winds and appropriately (and repeatedly) target the same cloud elements in time. Recall that a key assumption is that all clouds are assumed to propagate along the designated mean wind direction. Highly variable wind with time and, in the case of larger, more vigorous clouds, cloud development–decay alignment can play a critical role in a successful implementation of this methodology as an automated tracking system. While those assumptions for many shallow cloud types are likely viable, tracking algorithm design problems can be exacerbated by the narrow beamwidth of the Ka-SACR (0.3°) and other similar cloud radar systems. Moreover, at such small beamwidths, only small errors in establishing the mean horizontal wind direction can affect substantial losses in the quality and continuity of the

measurements (e.g., [appendix](#)). Different scanning strategies (including routine or reference sector scans) may also mitigate some of these known difficulties [e.g., boundary layer RHs; additional details on scan strategies are described in [Kollias et al. \(2014a\)](#)]. However, utilizing these scans to fill in spatial/azimuthal gaps implies a trade-off for adequate temporal revisiting of cloud elements for tracking and microphysical process monitoring.

A lingering concern when documenting several cloud parameters including cloud cross-sectional area (e.g., [Figs. 7–9](#)), is that it is likely that the CITA approach will underrepresent these values and/or should be further categorized according to additional spatial context. This concern is noted in response to cloud “chording” considerations with narrow-beam AW-RHI modes. These modes may not routinely sample the center of clouds, even if those clouds are properly established as propagating along the designated wind direction. When confronted with similar aircraft sampling chording problems, [Jorgensen et al. \(1985\)](#) derived that the measured diameter for a circular “core” target as a consequence of chording bias is expected to be approximately 22% low. A circular shape assumption for cumulus clouds may be applicable under low-shear shallow cumulus conditions (including those present during much of this MC3E event, e.g., [Fig. 2](#)). However, this diameter bias is arguably at the lower bound when considering the range of possible cumulus cloud forms and depths. One may extend a similar chording analysis to a generic ellipsoidal shape for a shallow cumulus cloud element. In this case, the chording bias will be more pronounced. For example, if the clouds are elongated along the wind direction and have an axis ratio (major to minor dimension) of 0.8, an expected bias in areal coverage (or calculation for forms of cloud fraction) would be approximately 32%. The potential implication on the monitoring of cloud mean, median, and maximum reflectivity behaviors is even less certain without additional study on spatial cloud behaviors and chording implications therein. At a minimum, the authors must recommend that future CITA-type scanning strategies consider periodic low-level PPI scans to better bound these horizontal-cloud-structure considerations.

Acknowledgments. The authors thank the reviewers whose insightful comments and suggestions enhance this manuscript. This paper has been authored by employees of Brookhaven Science Associates, LLC, under Contract DE-AC02-98CH10886 with the U.S. Department of Energy. The publisher by accepting the manuscript for publication acknowledges that the U.S. government retains a nonexclusive, paid-up, irrevocable, worldwide

license to publish or reproduce the published form of this manuscript, or allow others to do so, for U.S. government purposes. Author Giangrande’s work is supported by the U.S. Department of Energy, Office of Science, Office of Biological and Environmental Research (OBER) as part of the Atmospheric System Research (ASR) and ARM Programs. Additional author support was provided by the U.S. DOE ASR Program and by the BNL Laboratory Directed Research and Development (LDRD) Program.

APPENDIX

Sensitivity of CITA to In-Cloud Horizontal Wind Direction

The success of CITA depends in part on accurately determining the environmental/cloud-level wind direction to appropriately follow cloud elements in time. Considering a very simple advection model, any deviation from the cloud-level wind direction that the AW-RHI scan strategy can allow and still sample a similar volume will often depend on three parameters: the wind field at cloud level, the size of the region that can be assumed homogeneous, and the cloud life time. For this particular MC3E case, the wind field is not expected to significantly influence the results of CITA since only marginal shear is present that may allow clouds to propagate differently at different heights ([Fig. 2](#)). Given that the Ka-SACR beamwidth at a 10-km distance from the radar will be illuminating a sampling volume that is approximately a cylinder of ~50-m diameter, this is the size of the region that is assumed homogeneous for the following analysis.

If cloud elements are advected over the radar domain and have the middle point of cloud life cycle occurring as the cloud passes over the radar location, a maximum deviation for this AW-RHI radar scan angle from the cloud-level wind direction can be estimated ([Fig. A1](#)). It is noted that small errors in designating the horizontal wind direction can substantially impact the use of AW-RHI CITA techniques. When considering wind speeds less than 20 m s^{-1} ([Fig. 2](#)) and cloud lifetime shorter than 10 min ([Fig. 6](#)), the same cloud volume might be sampled approximately 20 times. However, one might only guarantee to capture the evolution of the same parcel if there is a variation of 1° between the scan angle and the cloud-level wind direction. If considering slower advection speeds of 10 m s^{-1} and shorter cloud life cycles, the allowable disagreement between the cloud-propagating direction and scan angle can be closer to 5° while still expecting to sample properties within the same small volume. Assuming that there are larger homogeneous cloud regions will also influence these results by allowing

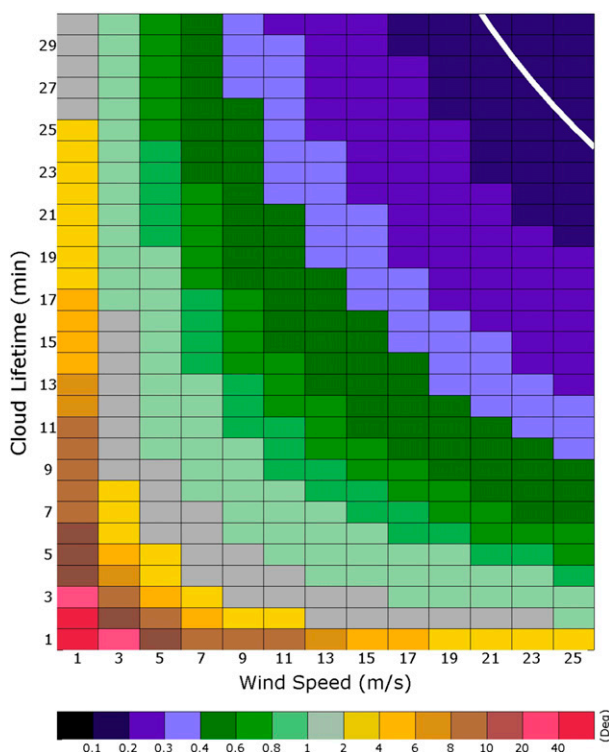


FIG. A1. Maximum deviation of the radar scan angle from the wind direction so that the radar measures variables within a homogeneous volume of 50-m diameter as a function of wind speed and cloud lifetime. The area in the top-right corner delimited by the thick white line represents the region where clouds cannot be observed given the time required to sample their full life cycle, the wind speed, and the domain size.

a larger disagreement between the angles. For example, if the homogeneous volume has a diameter of 100 m, then the deviation between the radar scan angle and the wind direction is roughly doubled that of the 50-m diameter.

REFERENCES

- Ackerman, T. A., and G. M. Stokes, 2003: The Atmospheric Radiation Measurement Program. *Phys. Today*, **56**, 38–45, doi:[10.1063/1.1554135](https://doi.org/10.1063/1.1554135).
- Boer, E., and V. Ramanathan, 1997: Lagrangian approach for deriving cloud characteristics from satellite observations and its implications to cloud parameterizations. *J. Geophys. Res.*, **102**, 21 383–21 399, doi:[10.1029/97JD00930](https://doi.org/10.1029/97JD00930).
- Burnet, F., and J.-L. Brenguier, 2010: The onset of precipitation in warm cumulus clouds: An observational case-study. *Quart. J. Roy. Meteor. Soc.*, **136**, 374–381, doi:[10.1002/qj.552](https://doi.org/10.1002/qj.552).
- Chen, S. S., R. A. Houze Jr., and B. E. Mapes, 1996: Multiscale variability of deep convection in relation to large-scale circulation in TOGA COARE. *J. Atmos. Sci.*, **53**, 1380–1409, doi:[10.1175/1520-0469\(1996\)053<1380:MVODCI>2.0.CO;2](https://doi.org/10.1175/1520-0469(1996)053<1380:MVODCI>2.0.CO;2).
- Dixon, M., and G. Wiener, 1993: TITAN: Thunderstorm Identification, Tracking, Analysis, and Nowcasting—A radar-based methodology. *J. Atmos. Oceanic Technol.*, **10**, 785–797, doi:[10.1175/1520-0426\(1993\)010<0785:TTITAA>2.0.CO;2](https://doi.org/10.1175/1520-0426(1993)010<0785:TTITAA>2.0.CO;2).
- Feingold, G., and H. Siebert, 2009: Cloud–aerosol interactions from the micro to the cloud scale. *Clouds in the Perturbed Climate System: Their Relationship to Energy Balance, Atmospheric Dynamics, and Precipitation*. J. Heintzenberg, and R. J. Charlson, Eds., Strüngmann Forum Rep. 2, MIT Press, 319–338.
- French, J. R., G. Vali, and R. D. Kelly, 1999: Evolution of small cumulus clouds in Florida: Observations of pulsating growth. *Atmos. Res.*, **52**, 143–165, doi:[10.1016/S0169-8095\(99\)00024-1](https://doi.org/10.1016/S0169-8095(99)00024-1).
- Futyan, J. M., and A. D. Del Genio, 2007: Deep convective system evolution over Africa and the tropical Atlantic. *J. Climate*, **20**, 5041–5060, doi:[10.1175/JCLI4297.1](https://doi.org/10.1175/JCLI4297.1).
- Ghan, S. J., L. R. Leung, and J. McCaa, 1999: A comparison of three different modeling strategies for evaluating cloud and radiation parameterizations. *Mon. Wea. Rev.*, **127**, 1967–1984, doi:[10.1175/1520-0493\(1999\)127<1967:ACOTDM>2.0.CO;2](https://doi.org/10.1175/1520-0493(1999)127<1967:ACOTDM>2.0.CO;2).
- Göke, S., H. T. Ochs, and R. M. Rauber, 2007: Radar analysis of precipitation initiation in maritime versus continental clouds near the Florida coast: Inferences concerning the role of CCN and giant nuclei. *J. Atmos. Sci.*, **64**, 3695–3707, doi:[10.1175/JAS3961.1](https://doi.org/10.1175/JAS3961.1).
- Grenier, H., and C. S. Bretherton, 2001: A moist PBL parameterization for large-scale models and its application to subtropical cloud-topped marine boundary layers. *Mon. Wea. Rev.*, **129**, 357–377, doi:[10.1175/1520-0493\(2001\)129<0357:AMPPFL>2.0.CO;2](https://doi.org/10.1175/1520-0493(2001)129<0357:AMPPFL>2.0.CO;2).
- Illingworth, A. J., and Coauthors, 2007: Cloudnet: Continuous evaluation of cloud profiles in seven operational models using ground-based observations. *Bull. Amer. Meteor. Soc.*, **88**, 883–898, doi:[10.1175/BAMS-88-6-883](https://doi.org/10.1175/BAMS-88-6-883).
- Johnson, J. T., P. L. MacKeen, A. Witt, E. D. Mitchell, G. J. Stumpf, M. D. Eilts, and K. W. Thomas, 1998: The storm cell identification and tracking algorithm: An enhanced WSR-88D algorithm. *Wea. Forecasting*, **13**, 263–276, doi:[10.1175/1520-0434\(1998\)013<0263:TSCIAT>2.0.CO;2](https://doi.org/10.1175/1520-0434(1998)013<0263:TSCIAT>2.0.CO;2).
- Jorgensen, D. P., E. J. Zipser, and M. A. LeMone, 1985: Vertical motions in intense hurricanes. *J. Atmos. Sci.*, **42**, 839–856, doi:[10.1175/1520-0469\(1985\)042<0839:VMIIH>2.0.CO;2](https://doi.org/10.1175/1520-0469(1985)042<0839:VMIIH>2.0.CO;2).
- Knight, C. A., and L. J. Miller, 1993: First radar echoes from cumulus clouds. *Bull. Amer. Meteor. Soc.*, **74**, 179–188, doi:[10.1175/1520-0477\(1993\)074<0179:FREFCC>2.0.CO;2](https://doi.org/10.1175/1520-0477(1993)074<0179:FREFCC>2.0.CO;2).
- , J. Vivekanandan, and S. G. Lasher-Trapp, 2002: First radar echoes and the early ZDR history of Florida cumulus. *J. Atmos. Sci.*, **59**, 1454–1472, doi:[10.1175/1520-0469\(2002\)059<1454:FREATE>2.0.CO;2](https://doi.org/10.1175/1520-0469(2002)059<1454:FREATE>2.0.CO;2).
- Kollias, P., E. E. Clothiaux, A. A. Miller, B. A. Albrecht, G. L. Stephens, and T. P. Ackerman, 2007: Millimeter-wavelength radars: New frontier in atmospheric cloud and precipitation research. *Bull. Amer. Meteor. Soc.*, **88**, 1608–1624, doi:[10.1175/BAMS-88-10-1608](https://doi.org/10.1175/BAMS-88-10-1608).
- , N. Bharadwaj, K. Widener, I. Jo, and K. Johnson, 2014a: Scanning ARM cloud radars. Part I: Operational sampling strategies. *J. Atmos. Oceanic Technol.*, **31**, 569–582, doi:[10.1175/JTECH-D-13-00044.1](https://doi.org/10.1175/JTECH-D-13-00044.1).
- , and Coauthors, 2014b: Scanning ARM cloud radars. Part II: Data quality control and processing. *J. Atmos. Oceanic Technol.*, **31**, 583–598, doi:[10.1175/JTECH-D-13-00045.1](https://doi.org/10.1175/JTECH-D-13-00045.1).
- Lu, M.-L., G. Feingold, H. H. Jonsson, P. Y. Chuang, H. Gates, R. C. Flagan, and J. H. Seinfeld, 2008: Aerosol–cloud relationships in continental shallow cumulus. *J. Geophys. Res.*, **113**, D15201, doi:[10.1029/2007JD009354](https://doi.org/10.1029/2007JD009354).

- Machado, L. A., W. B. Rossow, R. L. Guedes, and A. W. Walker, 1998: Life cycle variations of mesoscale convective systems over the Americas. *Mon. Wea. Rev.*, **126**, 1630–1654, doi:[10.1175/1520-0493\(1998\)126<1630:LCVOMC>2.0.CO;2](https://doi.org/10.1175/1520-0493(1998)126<1630:LCVOMC>2.0.CO;2).
- Maddox, R. A., 1980: Mesoscale convective complexes. *Bull. Amer. Meteor. Soc.*, **61**, 1374–1387, doi:[10.1175/1520-0477\(1980\)061<1374:MCC>2.0.CO;2](https://doi.org/10.1175/1520-0477(1980)061<1374:MCC>2.0.CO;2).
- Mather, J. H., and J. W. Voyles, 2013: The ARM Climate Research Facility: A review of structure and capabilities. *Bull. Amer. Meteor. Soc.*, **94**, 377–392, doi:[10.1175/BAMS-D-11-00218.1](https://doi.org/10.1175/BAMS-D-11-00218.1).
- Park, S., and C. S. Bretherton, 2009: The University of Washington shallow convection and moist turbulence schemes and their impact on climate simulations with the Community Atmosphere Model. *J. Climate*, **22**, 3449–3469, doi:[10.1175/2008JCLI2557.1](https://doi.org/10.1175/2008JCLI2557.1).
- Rosenfeld, D., 1987: Objective method for analysis and tracking of convective cells as seen by radar. *J. Atmos. Oceanic Technol.*, **4**, 422–434, doi:[10.1175/1520-0426\(1987\)004<0422:OMFAAT>2.0.CO;2](https://doi.org/10.1175/1520-0426(1987)004<0422:OMFAAT>2.0.CO;2).
- Stephens, G. L., 2005: Cloud feedbacks in the climate system: A critical review. *J. Climate*, **18**, 237–273, doi:[10.1175/JCLI-3243.1](https://doi.org/10.1175/JCLI-3243.1).
- Stevens, B., and G. Feingold, 2009: Untangling aerosol effects on clouds and precipitation in a buffered system. *Nature*, **461**, 607–613, doi:[10.1038/nature08281](https://doi.org/10.1038/nature08281).
- Stokes, G. M., and S. E. Schwartz, 1994: The Atmospheric Radiation Measurement (ARM) Program: Programmatic background and design of the Cloud and Radiation Testbed. *Bull. Amer. Meteor. Soc.*, **75**, 1201–1221, doi:[10.1175/1520-0477\(1994\)075<1201:TARMPP>2.0.CO;2](https://doi.org/10.1175/1520-0477(1994)075<1201:TARMPP>2.0.CO;2).
- Velasco, I., and J. M. Fritsch, 1987: Mesoscale convective complexes in the Americas. *J. Geophys. Res.*, **92**, 9591–9613, doi:[10.1029/JD092iD08p09591](https://doi.org/10.1029/JD092iD08p09591).
- Williams, M., and R. A. Houze, 1987: Satellite-observed characteristics of winter monsoon cloud clusters. *Mon. Wea. Rev.*, **115**, 505–519, doi:[10.1175/1520-0493\(1987\)115<0505:SOCOWM>2.0.CO;2](https://doi.org/10.1175/1520-0493(1987)115<0505:SOCOWM>2.0.CO;2).